INTERNATIONAL JOURNAL FOR NUMERICAL METHODS IN FLUIDS
Int. J. Numer. Meth. Fluids 2006; **52**:617–638
Published online 14 February 2006 in Wiley InterScience (www.interscience.wiley.com). DOI: 10.1002/fld.1190

A fully 3D finite volume method for incompressible Navier–Stokes equations

Alberto Deponti*,†, Vincenzo Pennati‡ and Lucia De Biase§

Environmental Science Department, University of Milano–Bicocca, Italy

SUMMARY

A semi-implicit numerical method for the three-dimensional incompressible Navier–Stokes equations is presented. The method describes the velocity and the non-hydrostatic pressure field and the free surface evolution in time. The governing equations are discretized by means of the finite volume method on a structured non-uniform grid; for this reason both local and global mass conservation are guaranteed. Convective and diffusive fluxes on the control volume faces, as well as boundary conditions, are approximated by high-order formulae. Copyright © 2006 John Wiley & Sons, Ltd.

KEY WORDS: Navier–Stokes; free surface; non-hydrostatic; three-dimensional; finite volume method; high-order approximations

1. INTRODUCTION

Aim of the present work is a description of the dynamics of three-dimensional environmental free surface flows; in particular, the work starts from the need to describe alpine glacier dynamics. Following some recent works (see References [1–5] among others), ice is considered a non-Newtonian fluid in which viscosity depends on the deformation field through a particular constitutive law (Glen's law); in this context, a fluid-dynamic approach is used and Navier–Stokes equations are considered.

Environmental flows are usually fully three-dimensional and non-hydrostatic due to the complex geometry of the domains (e.g. rivers, lakes and glaciers) and to the evolution of the free surface which explains why a fully three-dimensional modelling approach is needed. In this work a new fully three-dimensional semi-implicit method, applicable to generic environmental Newtonian and non-Newtonian fluids, is proposed and tested in two versions, namely with and

*Correspondence to: A. Deponti, Environmental Science Department, University of Milano–Bicocca, Italy.
†E-mail: alberto.deponti@unimib.it
‡E-mail: vpennati@email.it
§E-mail: lucia.debiase@unimib.it

Contract/grant sponsor: Fondazione Fratelli Confalonieri

Received 19 August 2004
Revised 12 April 2005
Accepted 3 January 2006

without modelling the free surface evolution. Of the two versions, the first directly calculates the full pressure field, while the second deals with the non-hydrostatic regime by splitting the pressure into two components and calculating the hydrostatic pressure component first and the hydrodynamic pressure component in a subsequent step.

Since in the description of free surface environmental flows, local and global mass conservation is crucial, the *finite volume* method is used. In order to properly describe the geometry of the domain and of the free surface, non-uniform control volumes are used. This allows *a priori adaptivity* of the solution by reducing the control volume dimensions where the domain geometry is particularly complex or where high gradients of the solution are expected. The adaptivity of the control volume dimensions and the topological information related to the space discretization are managed by a preprocessor written on purpose. New high-order approximations are used for the computation of convective and diffusive fluxes on the control volume faces (see the Appendix); boundary conditions are approximated by high-order generalized finite difference formulae [6, 7]. Two different schemes based on the *fractional step* method are proposed for time discretization of the field equations.

In the next section the governing equations are presented and subsequently the space and time discretizations are described. Finally, some fluid-dynamic applications are presented.

2. GOVERNING EQUATIONS

The dynamics of unsteady free surface flows is described by the three-dimensional Navier–Stokes equations that for an incompressible fluid, in conservation vector form are

$$\begin{gathered} \frac{\partial \mathbf{u}}{\partial t} + \nabla \cdot \{\mathbf{u}\mathbf{u} - \nu \nabla \mathbf{u}\} = -\nabla p + \mathbf{f} \\ \nabla \cdot \mathbf{u} = 0 \end{gathered} \tag{1}$$

where $\mathbf{u} = [u, v, w]^{\mathrm{T}}$ is the three-dimensional velocity vector, t is the time, $\nabla\cdot$ is the divergence operator, ∇ is the gradient operator, ν is the kinematic viscosity, p is the kinematic pressure and $\mathbf{f}$ represents the body forces divided by the fluid density. In this work only the gravity force will be considered, hence $\mathbf{f} = \mathbf{g}$.

The surface of the fluid is a stress-free surface that can evolve in time. At this boundary the kinematic boundary condition holds:

$$\frac{\partial \eta}{\partial t} + u \frac{\partial \eta}{\partial x} + v \frac{\partial \eta}{\partial y} - w = 0 \tag{2}$$

where η is the surface elevation above the undisturbed reference system. The lower boundary is not allowed to move in time, and therefore the tangency condition holds:

$$u \frac{\partial(-h)}{\partial x} + v \frac{\partial(-h)}{\partial y} - w = 0 \tag{3}$$

where h is the base depth. Integration of continuity equation from the base to the surface and substitution of Equations (2) and (3) lead to the Saint Venant equation:

$$\frac{\partial \eta}{\partial t} + \frac{\partial}{\partial x}\int_{-h}^{\eta} u\,\mathrm{d}z + \frac{\partial}{\partial y}\int_{-h}^{\eta} v\,\mathrm{d}z = 0 \tag{4}$$

This equation describes the free surface evolution in time as a function of the unit-discharges and incorporates the physical law of mass conservation; the problem, particularly the free surface evolution, can properly be described by using the conservation form of the field Equations (1) and discretization techniques such as the finite volume method [8] that guarantee both local and global conservation of mass and momentum.

3. SPACE DISCRETIZATION

The computational domain is discretized by means of cell-centred control volumes in the shape of parallelepipeds; their centres provide a structured grid of points. All unknown field variables are evaluated at grid points. Although the control volumes are labelled at their centre with a proper number as usually done in the finite element method, for clarity in the paper each control volume is labelled at its centre by the tern of indices ijk. The dimensions of each control volume are Δx_{ijk}, Δy_{ijk} and Δz_{ijk}. The volume horizontal dimensions are chosen on the basis of *a priori* knowledge of the domain peculiarities and are fixed throughout computation. The volume height is also fixed with the same criterion but, due to the free surface evolution, the height of those including it can change in time and it may be necessary to add or suppress some volumes; this is why the dimension Δz will be time-indexed from now on.

The integral form of the field equations is written for each control volume; by Green–Gauss theorem this leads to computing the surface integral of the fluxes (convective and diffusive), i.e. to summing up the contributions of each control volume face, calculated by the *integral mean value* theorem. Since the unknowns are computed at the grid points, the flux values on the volume faces have to be approximated. To this aim, high-order local profiles, involving a cloud of points in and out the control volume, are used and they are general enough to allow for non-uniform distances between couples of points in the cloud; the ratio of two consecutive distances can indeed vary in the range $[1/3, 3]$. As said above, pressure and velocity are evaluated on co-located grids. No checker-board effect is suffered thanks to high-order formulae involving more than two points, while this is often the case when two-point central schemes are used for the first derivatives, unless staggered grids are adopted [9, 10]. In the finite element context the checker-board effect is prevented by choosing functional spaces for the pressure–velocity pair that satisfy the LBB condition [11, 12]. High-order general formulae are used also for the approximation of boundary conditions. In order to take advantage of boundary conditions most and to maintain a high-order of approximation, boundary volumes include more than one grid point, namely the centre and the points at the intersection of the boundary with grid lines orthogonal to it. Although the solution is not directly computed at the boundary points, they belong to the stencils used for the approximations of boundary conditions and of fluxes on the faces close to the boundary.

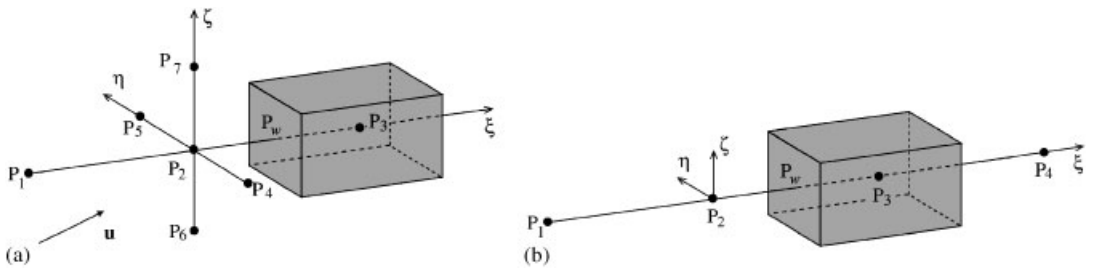

Figure 1. (a) Stencils for the approximation of the convective terms; and (b) of the diffusive terms. (ξ, η, ζ) is the local reference system used for the computation of numerical schemes.

In Figure 1(a) the seven-point stencil used to approximate the convective flux at point P_w is presented. The proposed profile is globally second-order accurate. The accuracy along the most relevant direction (ξ, orthogonal to the control volume face [13]) is of third order. Complete studies of convergence and stability properties in one and two dimensions were presented in References [14, 15]. The present method is the three-dimensional extension of those schemes. Being symmetric with respect to the ξ-direction, the stencil is easy to handle, even in the vicinity of the boundary. Whenever the spacing is uniform, this profile reduces to QUICK-3D [16].

In Figure 1(b) the four-point stencil used to approximate the diffusive flux at point P_w is presented. A central difference scheme is considered since diffusion is not a directional phenomenon and is not influenced by the velocity direction. The proposed profile is third-order accurate even in the case of non-uniform spacing.

Adequate rotations and translations of the two stencils allow the application to the other control volume faces. The coefficients for the calculation of convective and diffusive fluxes are presented in the Appendix.

4. TIME ADVANCING SCHEME

Numerical time integration of Navier–Stokes equations is often carried out by means of the *fractional step* method (or *projection* method) in which the equations are integrated in two or more steps. In the first step the velocity is computed by neglecting the divergence-free constraint. In the subsequent steps, mass conservation is imposed, in general, by solving a Poisson equation for the pressure. The fractional step method does not normally take the free surface into account. This is why for free surface problems a new scheme is proposed, while for rigid lid problems, in front of contrasting comments on performance and accuracy of projection schemes [17–27], a standard P1 technique is used. For stability reasons, a semi-implicit scheme is adopted for the momentum equation in the first step.

4.1. Type 1: rigid lid

When the surface evolution is not accounted for, the following two-step algorithm is considered.

In the first step the provisional velocities at time instant $n+1$, denoted by $\tilde{u}^{n+1}$, $\tilde{v}^{n+1}$ and $\tilde{w}^{n+1}$ are computed through the momentum equations by neglecting the pressure contribution:

$$\tilde{u}_{ijk}^{n+1}\Delta z_{ijk}^{n}+\frac{\Delta t}{\Delta x_{ijk}}\sum_{f=1}^{2}\left\{\left(u_{ijk}^{n}\tilde{u}_{ijk}^{n+1}-v_{ijk}^{n}\left[\frac{\partial\tilde{u}^{n+1}}{\partial x}\right]_{ijk}\right)\Delta z_{ijk}^{n}n_{x}\right\}_{f}+\frac{\Delta t}{\Delta y_{ijk}}\sum_{f=3}^{4}\left\{\left(v_{ijk}^{n}\tilde{u}_{ijk}^{n+1}-v_{ijk}^{n}\left[\frac{\partial\tilde{u}^{n+1}}{\partial y}\right]_{ijk}\right)\Delta z_{ijk}^{n}n_{y}\right\}_{f}+\Delta t\sum_{f=5}^{6}\left\{\left(w_{ijk}^{n}\tilde{u}_{ijk}^{n+1}-v_{ijk}^{n}\left[\frac{\partial\tilde{u}^{n+1}}{\partial z}\right]_{ijk}\right)n_{z}\right\}_{f}=F_{1} \tag{5}$$

$$\tilde{v}_{ijk}^{n+1}\Delta z_{ijk}^{n}+\frac{\Delta t}{\Delta x_{ijk}}\sum_{f=1}^{2}\left\{\left(u_{ijk}^{n}\tilde{v}_{ijk}^{n+1}-v_{ijk}^{n}\left[\frac{\partial\tilde{v}^{n+1}}{\partial x}\right]_{ijk}\right)\Delta z_{ijk}^{n}n_{x}\right\}_{f}+\frac{\Delta t}{\Delta y_{ijk}}\sum_{f=3}^{4}\left\{\left(v_{ijk}^{n}\tilde{v}_{ijk}^{n+1}-v_{ijk}^{n}\left[\frac{\partial\tilde{v}^{n+1}}{\partial y}\right]_{ijk}\right)\Delta z_{ijk}^{n}n_{y}\right\}_{f}+\Delta t\sum_{f=5}^{6}\left\{\left(w_{ijk}^{n}\tilde{v}_{ijk}^{n+1}-v_{ijk}^{n}\left[\frac{\partial\tilde{v}^{n+1}}{\partial z}\right]_{ijk}\right)n_{z}\right\}_{f}=F_{2} \tag{6}$$

$$\tilde{w}_{ijk}^{n+1}\Delta z_{ijk}^{n}+\frac{\Delta t}{\Delta x_{ijk}}\sum_{f=1}^{2}\left\{\left(u_{ijk}^{n}\tilde{w}_{ijk}^{n+1}-v_{ijk}^{n}\left[\frac{\partial\tilde{w}^{n+1}}{\partial x}\right]_{ijk}\right)\Delta z_{ijk}^{n}n_{x}\right\}_{f}+\frac{\Delta t}{\Delta y_{ijk}}\sum_{f=3}^{4}\left\{\left(v_{ijk}^{n}\tilde{w}_{ijk}^{n+1}-v_{ijk}^{n}\left[\frac{\partial\tilde{w}^{n+1}}{\partial y}\right]_{ijk}\right)\Delta z_{ijk}^{n}n_{y}\right\}_{f}+\Delta t\sum_{f=5}^{6}\left\{\left(w_{ijk}^{n}\tilde{w}_{ijk}^{n+1}-v_{ijk}^{n}\left[\frac{\partial\tilde{w}^{n+1}}{\partial z}\right]_{ijk}\right)n_{z}\right\}_{f}=F_{3} \tag{7}$$

where the right-hand sides are:

$$F_{1}=u_{ijk}^{n}\Delta z_{ijk}^{n}+g_{x}\Delta t\Delta z_{ijk}^{n} \tag{8}$$

$$F_{2}=v_{ijk}^{n}\Delta z_{ijk}^{n}+g_{y}\Delta t\Delta z_{ijk}^{n} \tag{9}$$

$$F_{3}=w_{ijk}^{n}\Delta z_{ijk}^{n}+g_{z}\Delta t\Delta z_{ijk}^{n} \tag{10}$$

Faces 1 and 2 of the control volume are orthogonal to the x-axis, faces 3 and 4 to the y-axis and faces 5 and 6 to the z-axis. The sums are extended to the control volume faces, the subscript f of the braces refers to quantities calculated on the control volume faces and n_x, n_y, n_z are the outward normals to the control volume faces. The physical boundary conditions

for the velocities are imposed. In the first step the continuity equation is not used so that the provisional velocity field is, in general, non-divergence free.

In the second step the final pressure p^{n+1} is calculated: the following form of the momentum equations is considered:

$$u_{ijk}^{n+1} = \tilde{u}_{ijk}^{n+1} - \Delta t \left[\frac{\partial p^{n+1}}{\partial x}\right]_{ijk} \tag{11}$$

$$v_{ijk}^{n+1} = \tilde{v}_{ijk}^{n+1} - \Delta t \left[\frac{\partial p^{n+1}}{\partial y}\right]_{ijk} \tag{12}$$

$$w_{ijk}^{n+1} = \tilde{w}_{ijk}^{n+1} - \Delta t \left[\frac{\partial p^{n+1}}{\partial z}\right]_{ijk} \tag{13}$$

The discrete mass conservation equation is

$$\frac{1}{\Delta x_{ijk}} \sum_{f=1}^{2} \{u_{ijk}^{n+1} \Delta z_{ijk}^{n} n_x\}_f + \frac{1}{\Delta y_{ijk}} \sum_{f=3}^{4} \{v_{ijk}^{n+1} \Delta z_{ijk}^{n} n_y\}_f + \sum_{f=5}^{6} \{w_{ijk}^{n+1} n_z\}_f = 0 \tag{14}$$

Formal substitution of Equations (11)–(13) into the mass conservation Equation (14) gives the following equation for the final pressure p^{n+1}:

$$\begin{aligned} \Delta t \left\{ \frac{1}{\Delta x_{ijk}} \sum_{f=1}^{2} \left\{ \left[\frac{\partial p^{n+1}}{\partial x}\right]_{ijk} \Delta z_{ijk}^{n} n_x \right\}_f + \frac{1}{\Delta y_{ijk}} \sum_{f=3}^{4} \left\{ \left[\frac{\partial p^{n+1}}{\partial y}\right]_{ijk} \Delta z_{ijk}^{n} n_y \right\}_f \right. \\ \left. + \sum_{f=5}^{6} \left\{ \left[\frac{\partial p^{n+1}}{\partial z}\right]_{ijk} n_z \right\}_f \right\} = \frac{1}{\Delta x_{ijk}} \sum_{f=1}^{2} \{\tilde{u}_{ijk}^{n+1} \Delta z_{ijk}^{n} n_x\}_f \\ + \frac{1}{\Delta y_{ijk}} \sum_{f=3}^{4} \{\tilde{v}_{ijk}^{n+1} \Delta z_{ijk}^{n} n_y\}_f + \sum_{f=5}^{6} \{\tilde{w}_{ijk}^{n+1} n_z\}_f \end{aligned} \tag{15}$$

As usually done in this method [17], homogeneous Neumann boundary conditions for the pressure are applied on boundaries where Dirichlet boundary conditions for the velocity are used and Dirichlet boundary conditions for the pressure are applied on boundaries where Neumann boundary conditions for the velocity are used.

The final velocities are calculated by Equations (11)–(13). Since the continuity equation has been imposed in the second step, the final velocity field is divergence free.

4.2. Type 2: free surface evolution

When the free surface evolution is considered, the time advancing scheme has to account for it. The free surface algorithm takes its start from Reference [24] but several differences can be highlighted:

- high-order formulae for both convective and diffusive terms replace lower-order approximations;

- implicit approximations for diffusive terms and semi-implicit for convective terms replace explicit approximations (vertical diffusive terms excepted) in the momentum equation;
- direct solution of the momentum equation in the first step implies a complete and direct exploitation of boundary conditions for the velocity; and
- the finite volume method is used for the discretization of all the field equations.

The high-order approximations lead to a system matrix with irregular pattern; in order to keep the fill-in low and to obtain accurate results, a specifically devised direct method is used [28].

The total kinematic pressure is divided into a hydrostatic part $g(\eta - z)$, which directly depends on the surface elevation, and a hydrodynamic part π:

$$p = g(\eta - z) + \pi \tag{16}$$

In the first step the provisional velocities are calculated by neglecting the contribution of the hydrodynamic pressure but considering the contribution of the hydrostatic pressure at the preceding time-step n. In this case, Equations (5)–(7) hold with the following right-hand sides:

$$F_1 = u_{ijk}^n \Delta z_{ijk}^n + \Delta t \Delta z_{ijk}^n \left\{ - \left[\frac{\partial \eta^n}{\partial x} \right]_{ij} + g_x \right\} \tag{17}$$

$$F_2 = v_{ijk}^n \Delta z_{ijk}^n + \Delta t \Delta z_{ijk}^n \left\{ - \left[\frac{\partial \eta^n}{\partial y} \right]_{ij} + g_y \right\} \tag{18}$$

$$F_3 = w_{ijk}^n \Delta z_{ijk}^n + \Delta t \Delta z_{ijk}^n (g + g_z) \tag{19}$$

After the provisional velocities are calculated, the provisional free surface elevation is calculated by the discretized form of Saint Venant Equation (4):

$$\tilde{\eta}_{ij}^{n+1} = \eta_{ij}^n - \sum_{k=m}^{M} \left(\frac{\Delta t}{\Delta x_{ij}} \sum_{f=1}^{2} \{ \tilde{u}_{ijk}^{n+1} \Delta z_{ijk}^n n_x \}_f + \frac{\Delta t}{\Delta y_{ij}} \sum_{f=3}^{4} \{ \tilde{v}_{ijk}^{n+1} \Delta z_{ijk}^n n_y \}_f \right) \tag{20}$$

where the k-indexed sum is extended over a column of volumes, from the base (index m) to the surface of the domain (index M).

In the second step the hydrodynamic pressure π is considered. In the presence of a moving surface, the discrete form of the mass conservation Equation (14) holds only for the control volumes not including the free surface, i.e. for $k = m, m+1, \ldots, M-1$; thus, with the same calculations presented in Section 4.1, the following equation for the hydrodynamic pressure π^{n+1} for $k = m, m+1, \ldots, M-1$ is obtained

$$\Delta t \left\{ \frac{1}{\Delta x_{ijk}} \sum_{f=1}^{2} \left\{ \left[\frac{\partial \pi^{n+1}}{\partial x} \right]_{ijk} \Delta z_{ijk}^n n_x \right\}_f + \frac{1}{\Delta y_{ijk}} \sum_{f=3}^{4} \left\{ \left[\frac{\partial \pi^{n+1}}{\partial y} \right]_{ijk} \Delta z_{ijk}^n n_y \right\}_f + \sum_{f=5}^{6} \left\{ \left[\frac{\partial \pi^{n+1}}{\partial z} \right]_{ijk} n_z \right\}_f \right\}$$

$$= \frac{1}{\Delta x_{ijk}} \sum_{f=1}^{2} \{ \tilde{u}_{ijk}^{n+1} \Delta z_{ijk}^n n_x \}_f + \frac{1}{\Delta y_{ijk}} \sum_{f=3}^{4} \{ \tilde{v}_{ijk}^{n+1} \Delta z_{ijk}^n n_y \}_f + \sum_{f=5}^{6} \{ \tilde{w}_{ijk}^{n+1} n_z \}_f \tag{21}$$

In order to calculate the hydrodynamic pressure π^{n+1} on the surface control volumes together with the final free surface elevation, Equation (20) is considered but the final surface elevation η_{ij}^{n+1} replaces the provisional surface elevation $\tilde{\eta}_{ij}^{n+1}$. Formal substitution of Equation (14) into this equation for η_{ij}^{n+1} gives

$$\frac{\eta_{ij}^{n+1}-\eta_{ij}^{n}}{\Delta t}+\frac{1}{\Delta x_{ijM}}\sum_{f=1}^{2}\{u_{ijM}^{n+1}\Delta z_{ijM}^{n}n_x\}_f + \frac{1}{\Delta y_{ijM}}\sum_{f=3}^{4}\{v_{ijM}^{n+1}\Delta z_{ijM}^{n}n_y\}_f+\{(w_{ijM}^{n+1}-w_{ijm}^{n+1})n_z\}_{f=5}=0 \tag{22}$$

The following form of the momentum equations is considered:

$$u_{ijk}^{n+1}=\tilde{u}_{ijk}^{n+1}-\Delta t\left[\frac{\partial\pi^{n+1}}{\partial x}\right]_{ijk} \tag{23}$$

$$v_{ijk}^{n+1}=\tilde{v}_{ijk}^{n+1}-\Delta t\left[\frac{\partial\pi^{n+1}}{\partial y}\right]_{ijk} \tag{24}$$

$$w_{ijk}^{n+1}=\tilde{w}_{ijk}^{n+1}-\Delta t\left[\frac{\partial\pi^{n+1}}{\partial z}\right]_{ijk} \tag{25}$$

Substitution into Equation (22) gives

$$\begin{aligned}\frac{\eta_{ij}^{n+1}}{\Delta t}-\Delta t\Bigg\{&\frac{1}{\Delta x_{ijM}}\sum_{f=1}^{2}\left\{\left[\frac{\partial\pi^{n+1}}{\partial x}\right]_{ijM}\Delta z_{ijM}^{n}n_x\right\}_f\\&+\frac{1}{\Delta y_{ijM}}\sum_{f=3}^{4}\left\{\left[\frac{\partial\pi^{n+1}}{\partial y}\right]_{ijM}\Delta z_{ijM}^{n}n_y\right\}_f+\left\{\left[\frac{\partial\pi^{n+1}}{\partial z}\right]_{ijM}n_z\right\}_{f=5}\Bigg\}\\=\frac{\eta_{ij}^{n}}{\Delta t}-\Bigg\{&\frac{1}{\Delta x_{ijM}}\sum_{f=1}^{2}\{\tilde{u}_{ijM}^{n+1}\Delta z_{ijM}^{n}n_x\}_f+\frac{1}{\Delta y_{ijM}}\sum_{f=3}^{4}\{\tilde{v}_{ijM}^{n+1}\Delta z_{ijM}^{n}n_y\}_f+\{(\tilde{w}_{ijM}^{n+1}-\tilde{w}_{ijm}^{n+1})n_z\}_{f=5}\Bigg\}\end{aligned} \tag{26}$$

In Equation (26) two unknowns are present: the new surface elevation η_{ij}^{n+1} and the hydrodynamic pressure in the surface control volumes π_{ijM}^{n+1}. In order to solve this equation, the pressure in the surface control volumes is considered hydrostatic, i.e. $g(\eta^{n+1}-z)=g(\tilde{\eta}^{n+1}-z)+\pi^{n+1}$, whence:

$$\eta^{n+1}=\tilde{\eta}^{n+1}+\frac{\pi^{n+1}}{g} \tag{27}$$

Substitution of Equation (27) into Equation (26) gives the equation for the hydrodynamic pressure in the surface control volumes:

$$
\begin{aligned}
-\frac{\pi_{ijM}^{n+1}}{g\Delta t}+\Delta t\Bigg\{&\frac{1}{\Delta x_{ijM}}\sum_{f=1}^{2}\left\{\left[\frac{\partial\pi^{n+1}}{\partial x}\right]_{ijM}\Delta z_{ijM}^{n}n_x\right\}_f\\
&+\frac{1}{\Delta y_{ijM}}\sum_{f=3}^{4}\left\{\left[\frac{\partial\pi^{n+1}}{\partial y}\right]_{ijM}\Delta z_{ijM}^{n}n_y\right\}_f+\left\{\left[\frac{\partial\pi^{n+1}}{\partial z}\right]_{ijM}n_z\right\}_{f=5}\Bigg\}\\
=&\frac{\tilde{\eta}_{ij}^{n+1}-\eta_{ij}^{n}}{\Delta t}+\Bigg\{\frac{1}{\Delta x_{ijM}}\sum_{f=1}^{2}\{\tilde{u}_{ijM}^{n+1}\Delta z_{ijM}^{n}n_x\}_f+\frac{1}{\Delta y_{ijM}}\sum_{f=3}^{4}\{\tilde{v}_{ijM}^{n+1}\Delta z_{ijM}^{n}n_y\}_f\\
&+\{(\tilde{w}_{ijM}^{n+1}-\tilde{w}_{ijm}^{n+1})n_z\}_{f=5}\Bigg\}
\end{aligned}
\tag{28}
$$

The hydrodynamic pressure is calculated by Equations (21) and (28) with homogeneous Neumann boundary conditions at all boundaries.

After the hydrodynamic pressure is calculated, the final velocity field is computed by Equations (23)–(25) and the final free surface elevation is computed by Equation (27). As in the preceding algorithm, the final velocity field is divergence free since the mass conservation has been imposed in the second step; moreover, the free surface elevation is consistent with the inner velocity field since the Saint Venant equation has been used.

5. APPLICATIONS

5.1. Analytical test

In the first application the exact fully three-dimensional solution presented in Reference [29] is considered:

$$u=-a[\mathrm{e}^{ax}\sin(ay\pm bz)+\mathrm{e}^{az}\cos(ax\pm by)]\mathrm{e}^{-b^2t} \tag{29}$$

$$v=-a[\mathrm{e}^{ay}\sin(az\pm bx)+\mathrm{e}^{ax}\cos(ay\pm bz)]\mathrm{e}^{-b^2t} \tag{30}$$

$$w=-a[\mathrm{e}^{az}\sin(ax\pm by)+\mathrm{e}^{ay}\cos(az\pm bx)]\mathrm{e}^{-b^2t} \tag{31}$$

$$
\begin{aligned}
p=-\frac{a^2}{2}[&\mathrm{e}^{2ax}+\mathrm{e}^{2ay}+\mathrm{e}^{2az}+2\sin(ax\pm by)\cos(az\pm bx)\mathrm{e}^{a(y+z)}\\
&+2\sin(ay\pm bz)\cos(ax\pm by)\mathrm{e}^{a(x+z)}+2\sin(az\pm bx)\cos(ay\pm bz)\mathrm{e}^{a(x+y)}]\mathrm{e}^{-2b^2t}
\end{aligned}
\tag{32}
$$

where $a=\pi/4$ and $b=\pi/2$. The computational domain is a unitary cube where $0\leqslant x\leqslant 1$, $0\leqslant y\leqslant 1$ and $-1\leqslant z\leqslant 0$. The domain has been discretized by 1008 control volumes of dimensions $\Delta x=\Delta y=0.083$, $\Delta z=0.143$. Since the surface does not change in time, the first

time advancing scheme is used (Section 4.1); the calculation has been carried out for 1000 time-steps with $\Delta t = 0.003$. In order to make the results comparable to those presented in Reference [29] we work in the same conditions, i.e. the kinematic viscosity has been set to unity, the initial conditions ($t = 0$) have been imposed using Equations (29)–(32) and Dirichlet boundary conditions have been imposed on all boundaries for velocity and pressure by Equations (29)–(32).

In Figure 2(a) the calculated velocity field at time $t = 0.3$ in the central longitudinal section of the domain ($y = 0.5$) is compared with the exact velocity field at the same time instant in the same section (Figure 2(b)). From these figures it can be noticed that the calculated velocity field coincides with the exact one and also that the flow field is rather complex and not unidirectional, thus providing a good test case. In Figure 3(a) the time history of the ℓ^2 difference norm for velocity $\varepsilon_{\mathbf{u}}$ and pressure ε_p are presented. The discrete ℓ^2 norm for velocity is computed by

$$\varepsilon_{\mathbf{u}} = \sqrt{\sum_{\text{vol}} \left(\Delta x \Delta y \Delta z \sum_{i=1}^{3} (u_i - \hat{u}_i)^2 \right)_{\text{vol}}} \tag{33}$$

where the outer sum is extended to all control volumes, Δx, Δy, Δz are the dimensions of the control volume, u_i and $\hat{u}_i$ are the three components of the numerically computed velocity and of the exact velocity, respectively. The discrete ℓ^2 norm of the pressure is computed by

$$\varepsilon_p = \sqrt{\sum_{\text{vol}} (\Delta x \Delta y \Delta z (p - \hat{p})^2)_{\text{vol}}} \tag{34}$$

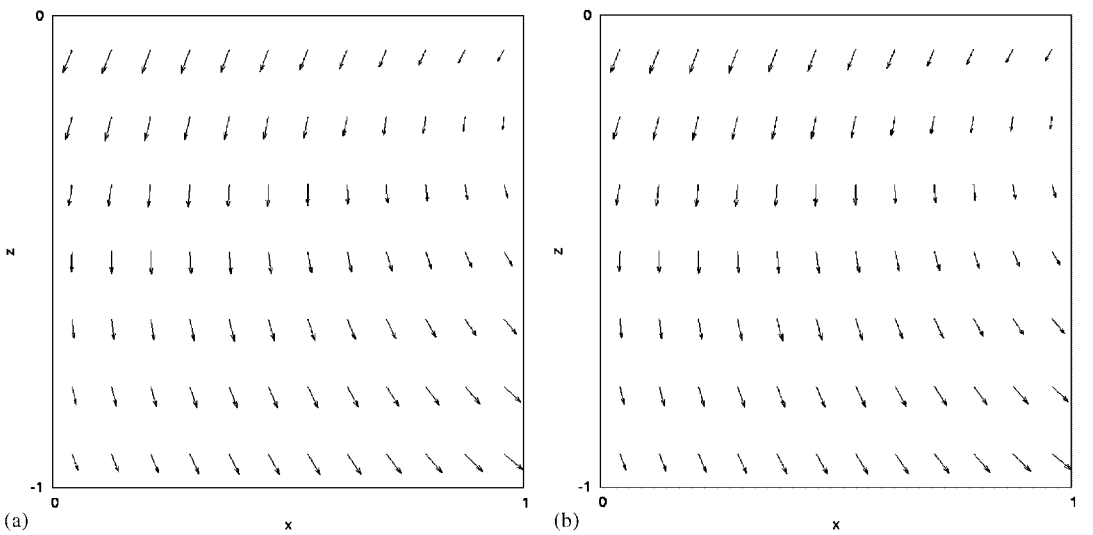

Figure 2. (a) Numerically computed; and (b) exact velocity field at $t = 0.3$ in the central transverse section of the computational domain ($y = 0.5$).

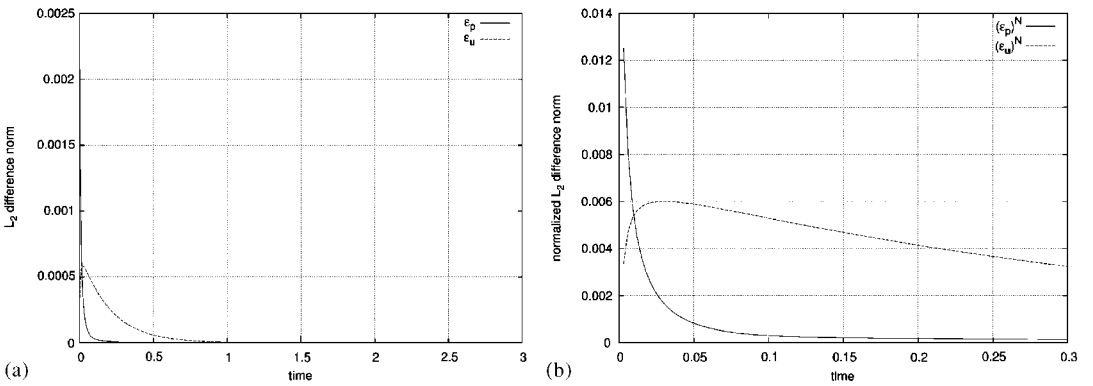

Figure 3. (a) Time history of the ℓ^2 difference norms of the velocity field $\varepsilon_{\mathbf{u}}$ and of the pressure ε_p until time instant $t=3$ for a total of 1000 time-steps; and (b) time history of the normalized ℓ^2 difference norms of the velocity field $(\varepsilon_{\mathbf{u}})^{\mathrm{N}}$ and of the pressure $(\varepsilon_p)^{\mathrm{N}}$ until time instant $t=0.3$; to be noted that for $t>0.3$, both velocity and pressure decrease very quickly so that the normalized ℓ^2 difference norm loses sense.

It can be seen that the difference norm is always very small and rapidly decreases for increasing time; moreover, no numerical instability or computational error dispersion can be noticed. In Figure 3(b) the time history until time $t=0.3$ of the normalized ℓ^2 difference norm of velocity $(\varepsilon_{\mathbf{u}})^{\mathrm{N}}$ and pressure $(\varepsilon_p)^{\mathrm{N}}$ are presented; these are calculated by

$$(\varepsilon_{\mathbf{u}})^{\mathrm{N}}=\frac{\sqrt{\sum_{\mathrm{vol}}\Delta x\Delta y\Delta z\ \sum_{i=1}^{3}(u_i-\hat{u}_i)^2}}{\sqrt{\sum_{\mathrm{vol}}\Delta x\Delta y\Delta z\ \sum_{i=1}^{3}(\hat{u}_i)^2}} \tag{35}$$

$$(\varepsilon_p)^{\mathrm{N}}=\frac{\sqrt{\sum_{\mathrm{vol}}\Delta x\Delta y\Delta z(p-\hat{p})^2}}{\sqrt{\sum_{\mathrm{vol}}\Delta x\Delta y\Delta z\,\hat{p}^2}} \tag{36}$$

It can be noticed that also the normalized difference norms are always very small. In particular, it can be noticed that at time $t=0.1$ the normalized ℓ^2 difference norms are $(\varepsilon_{\mathbf{u}})^{\mathrm{N}}=5\times10^{-3}$ and $(\varepsilon_p)^{\mathrm{N}}=3\times10^{-4}$; the result for the velocity is comparable to that presented in Reference [29] while the result for the pressure is better.

5.2. *Oscillating basin*

In the second test a standing wave in a basin is considered; this test has been solved by different authors with minor modifications [24, 27, 30–32]. Here a square basin of length $L=10\,\mathrm{m}$ and depth $h=10\,\mathrm{m}$ is considered. Even if the problem is two dimensional, the basin has been considered 2.5 m thick so that it has been modelled in three dimensions. The initial profile of the free surface is described by

$$\eta(x)=a\cos\left(\frac{2\pi x}{\lambda}\right) \tag{37}$$

where $a = 0.1\text{m}$ is the wave amplitude and $\lambda = 2L$ is the wavelength. Since the wave amplitude is small compared to the total depth, the wave celerity can be approximated by [24]

$$c = \sqrt{\frac{g\lambda}{2\pi} \tanh\left(\frac{2\pi h}{\lambda}\right)} \tag{38}$$

In this test the free surface evolves in time, thus the second time advancing scheme is used (Section 4.2); moreover, the hydrodynamic pressure plays here a fundamental role due to the presence of vertical accelerations.

The problem has been non-dimensionalized considering the scale L for the lengths and c for the velocities; the pressure has been non-dimensionalized with the scale c^2, the gravity acceleration with the scale c^2/L and time with the scale L/c. The computational domain has been discretized by 757 control volumes. The control volume dimensions in the x- and y-directions are fixed and uniform ($\Delta x = 0.048$, $\Delta y = 0.083$) while the dimensions in the z-direction are non-uniform; in particular, the lower volumes have a height of 0.116 non-dimensional units while the upper volumes have a height of 0.06 non-dimensional units; finally, the surface control volumes height is allowed to vary in time.

Perfect slip conditions are applied on solid walls and the stress-free condition is applied at the surface. Homogeneous Neumann boundary conditions for the hydrodynamic pressure are applied at all boundaries.

Results for an inviscid fluid and $\Delta t = 0.001$ are presented in Figure 4. It can be noticed that the model is stable even with no viscosity and that only a very small wave amplitude attenuation is obtained; in this simulation no mass loss has been detected. By graphical comparison with References [24, 27], it can be noticed that the wave attenuation is much lower.

Tests with different values of the kinematic viscosity have been performed: in Figure 5 the time history of the surface elevation at $x = 0$ for $v = 0.1, 0.01, 0.001$ corresponding to $Re = 10, 100, 1000$ are presented; $\Delta t = 0.01$ has been used for the simulations with $v = 0.1$

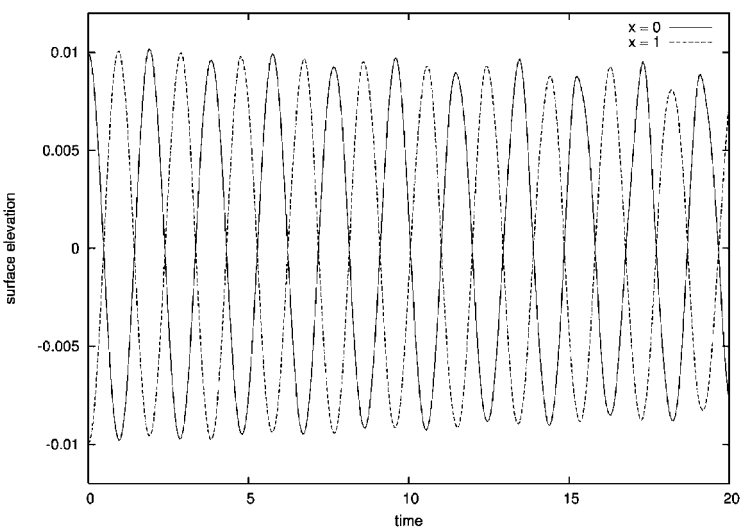

Figure 4. Time history of the free surface evolution at $x = 0$ and 1 for an inviscid fluid.

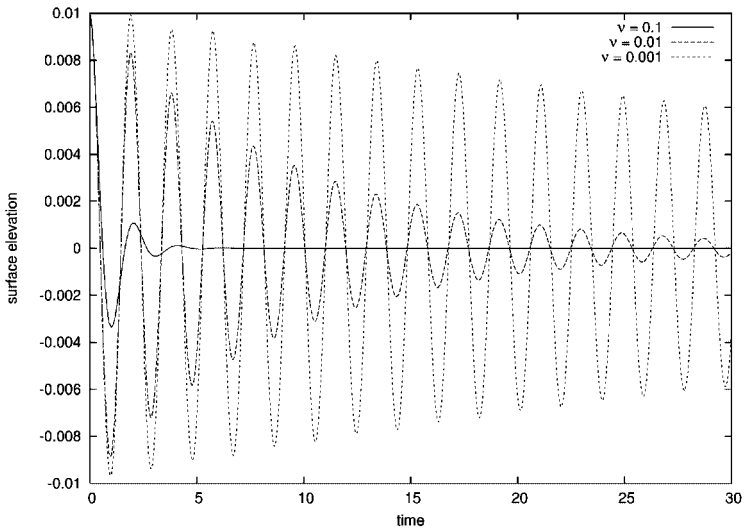

Figure 5. Time history of the free surface evolution at $x = 0$ for $v = 0.1, 0.01, 0.001$ corresponding to $Re = 10, 100, 1000$.

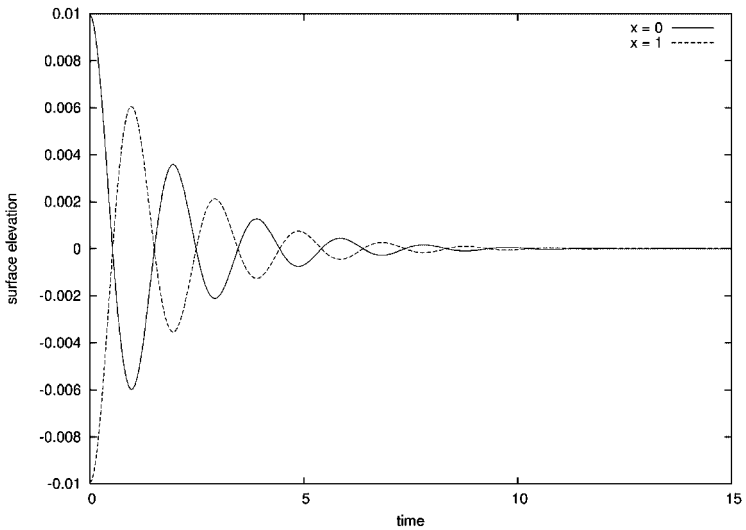

Figure 6. Time history of the free surface evolution at $x = 0$ and 1.

and $v = 0.01$, while $\Delta t = 0.001$ has been used for the simulation with $v = 0.001$. The results show attenuation of the wave amplitude due to viscous effects that agree with the physics of the problem and with the results presented in References [30, 31]. The solution is globally stable and converges to the undisturbed steady solution. Results obtained with $v = 0.05$ and $\Delta t = 0.01$ are presented in detail. In Figure 6 the time history of the surface evolution at $x = 0$ and 1

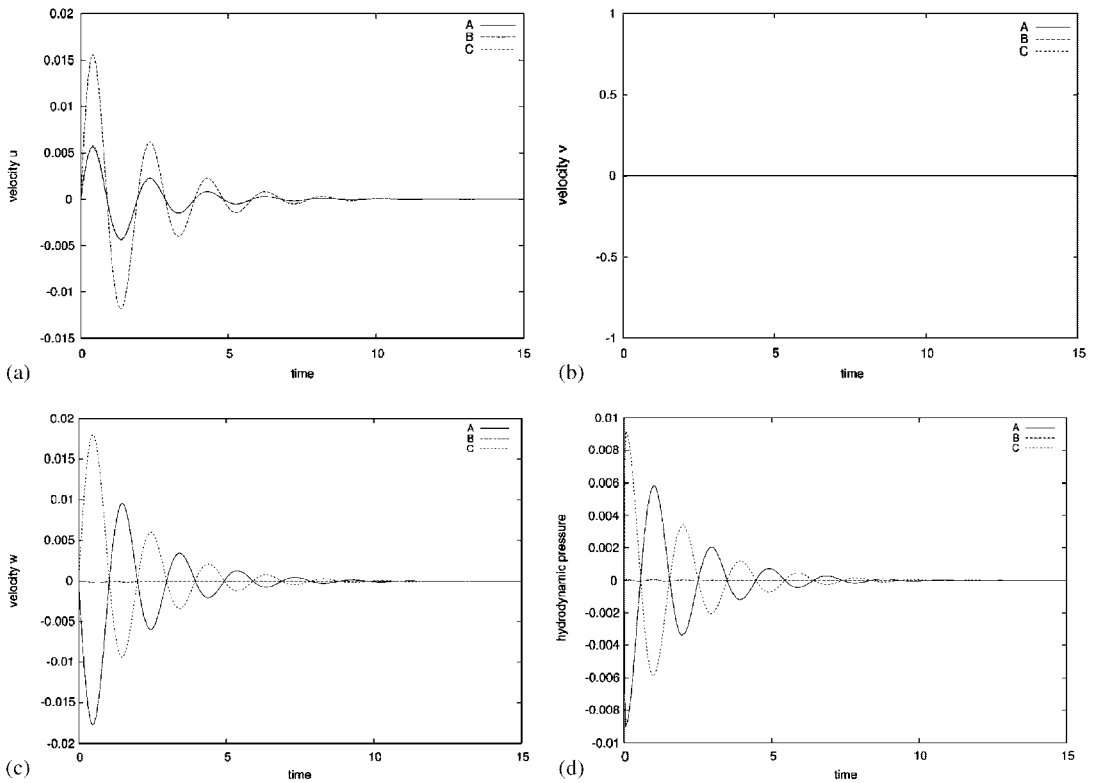

Figure 7. Time history of the velocity and hydrodynamic pressure at three control points near the surface: $A \equiv (0.120, 0.125, -0, 150)$, $B \equiv (0.500, 0.125, -0, 150)$, $C \equiv (0.880, 0.125, -0, 150)$. (a) The evolution of the horizontal velocity u is presented; (b) the evolution of the transverse velocity v; (c) the evolution of the vertical velocity w; and (d) the evolution of the hydrodynamic pressure.

is presented: the attenuation of the wave amplitude can be appreciated. In Figure 7 the time history of the evolution of the three components of the velocity field and of the hydrodynamic pressure at three control points near the surface are presented. It can be noticed that the horizontal velocity u and the vertical velocity w oscillate and change directions in agreement with the free surface evolution; moreover, it can be noticed that the transverse velocity v is always null as expected. Finally, the importance of the hydrodynamic component in the evolution of the motion field and of the free surface can be appreciated in Figure 7(d). In Figure 8 the free surface geometry and the velocity and pressure fields in the central vertical section of the domain at two different time instants are presented. In particular, it can be seen how the motion field inverts direction from $t = 0.25$ to 1.25 and how the hydrodynamic pressure drives the free surface evolution. In all the simulations no appreciable mass loss has been detected.

All the tests considered in the cited literature use a small wave amplitude (i.e. 1% of the basin depth); we have been unable to find larger amplitudes. In the following tests a

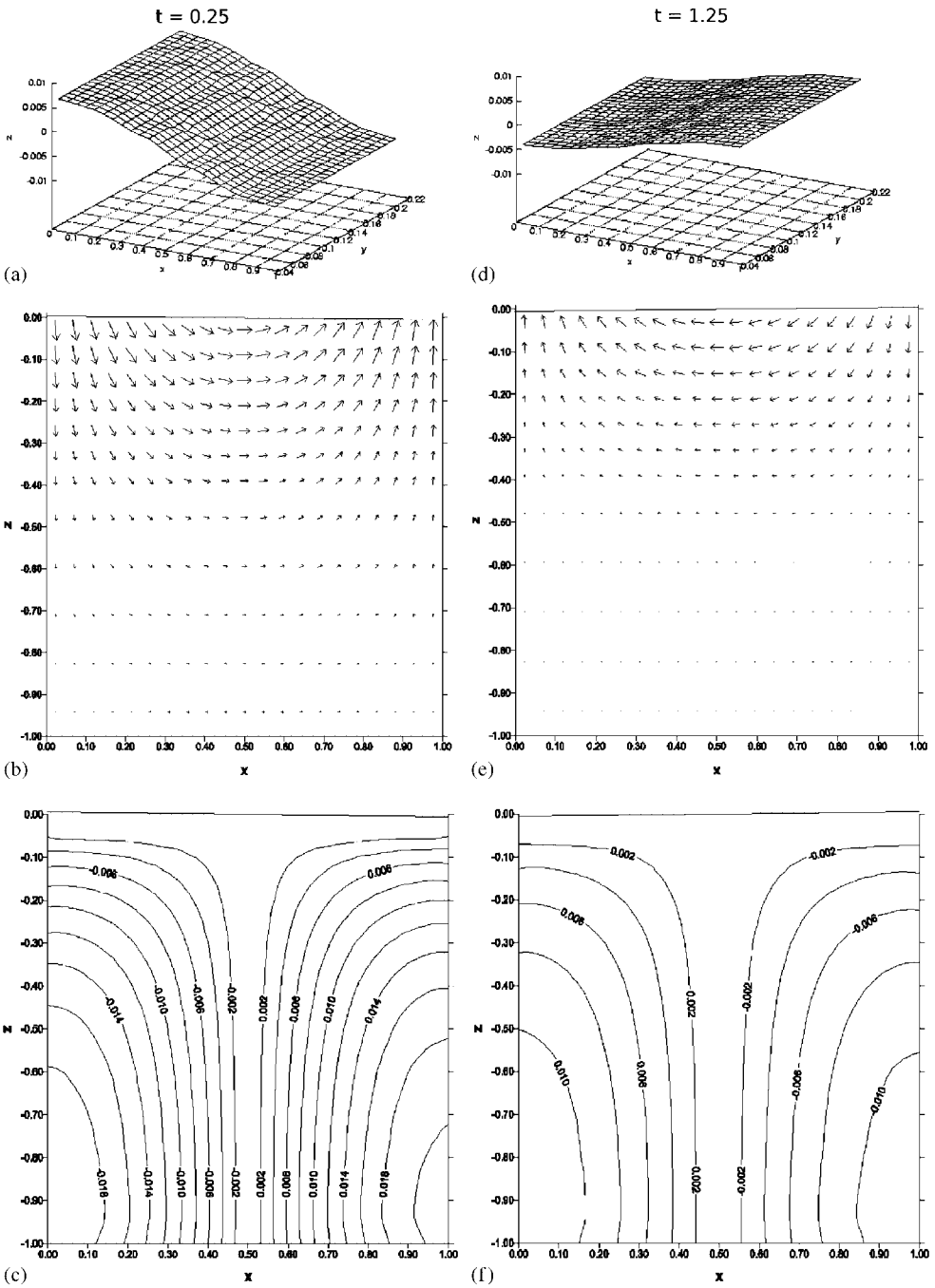

Figure 8. (a,d) Free surface geometry; (b,e) velocity; and (c,f) pressure fields in the central vertical section of the domain at time $t = 0.25$ and 1.25, respectively.

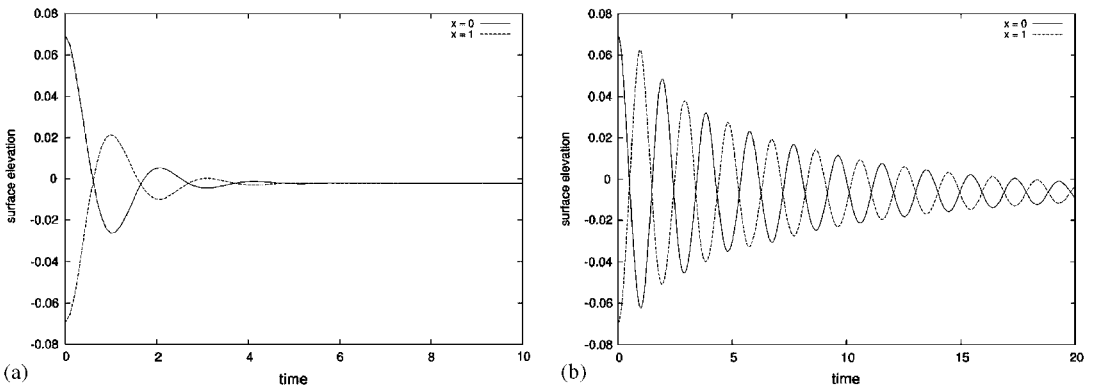

Figure 9. (a) Time history of the free surface evolution at $x = 0$ and 1 for $v = 0.1$; and (b) $v = 0.01$ with a wave amplitude $a = 0.07$.

bigger wave amplitude (i.e. 7% of the basin depth) is considered. In this case, the flow regime is non-hydrostatic and up to three volume layers are affected by the free surface evolution. Results of the simulations with $v = 0.1$ and 0.01 and $\Delta t = 0.01$ are presented in Figure 9. In the simulation with $v = 0.1$, at time $t = 20$, a mass loss of 0.2% is detected, while in the simulation with $v = 0.01$, at time $t = 10$, a mass loss of 0.5% is detected; these small mass losses are most probably caused by the geometric description of the free surface evolution.

5.3. *Three-dimensional oscillating basin*

In the following application a three-dimensional free surface flow is modelled. A basin of length $L_x = 10$ m, width $L_y = 5$ m and depth $h = 10$ m is considered. The initial profile of the free surface is described by:

$$\eta(x, y) = \frac{a}{2}\left[\cos\left(\frac{2\pi x}{\lambda_x}\right) + \cos\left(\frac{2\pi x}{\lambda_y}\right)\right] \tag{39}$$

where $a = 0.1$ is the wave amplitude, $\lambda_x = 2L_x$ and $\lambda_y = 2L_y$ are the two wavelengths. As in the previous test the second time advancing scheme is used. The problem has been non-dimensionalized considering the scale L_x for the lengths and the scale $c = \sqrt{(g\lambda_x/2\pi)\tanh(2\pi h/\lambda_x)}$ for the velocities; the pressure has been non-dimensionalized with the scale c^2, the gravity acceleration with the scale c^2/L_x and time with the scale L_x/c. The computational domain has been discretized by 1512 control volumes. The horizontal dimensions of the control volumes are $\Delta x = 0.048$ and $\Delta y = 0.083$ non-dimensional units; the vertical dimensions are non-uniform; in particular the lower volumes have a height of 0.093 non-dimensional units while the upper volumes have a height of 0.05 non-dimensional units; moreover, the surface control volumes heights are allowed to vary in time. Perfect slip conditions are applied on solid walls and the stress-free condition is applied at the surface. Homogeneous Neumann boundary conditions for the hydrodynamic pressure are

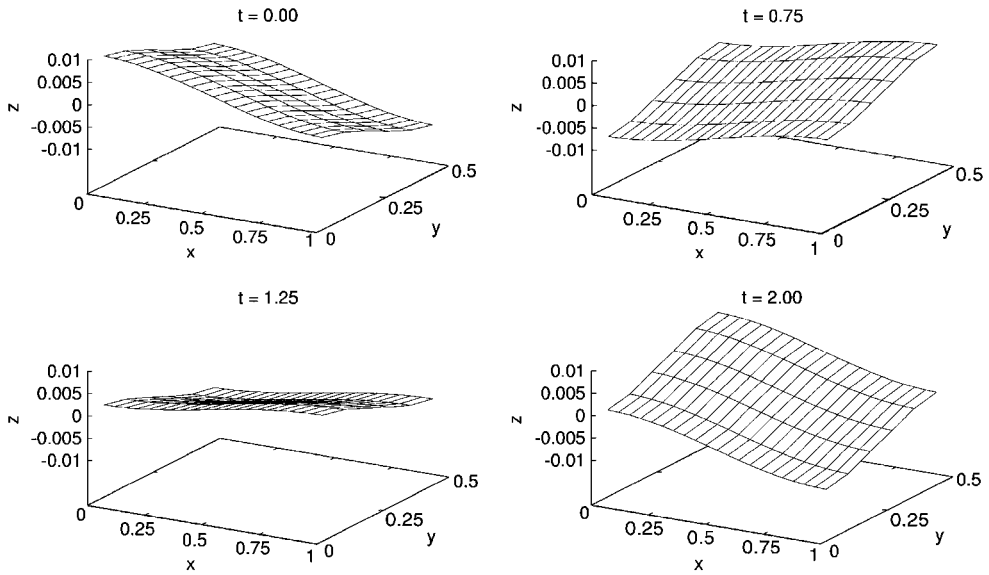

Figure 10. Surface elevation at four time instants.

applied at all boundaries. An inviscid fluid is considered. In Figure 10 the free surface geometries at four different time instants are presented. It can be noticed that the surface geometry is fully three-dimensional and that at each time instant one of the four vertexes reaches the maximum. In Figure 11 the time histories of free surface, pressure and velocity at two control points are presented. The control points for the free surface are $P1 \equiv (0.024, 0.042)$ and $P2 \equiv (0.976, 0.458)$; those for pressure and velocity are $P3 \equiv (0.024, 0.042, -0.025)$ and $P4 \equiv (0.976, 0.458, -0.025)$. From the time history of the surface evolution and of the hydrodynamic pressure evolution, the wave interaction can be appreciated; these interactions are created by the superposition of waves travelling in different directions with different velocities and being reflected by the walls of the basin. Form the time history of the velocity components evolution, the three-dimensionality of the problem can be appreciated: the three velocity components are always comparable and none vanishes. Finally, it can be noticed that the free surface evolution is in agreement with the hydrodynamic pressure and with the vertical velocity component.

In addition to the inviscid case, a test with a non-dimensional kinematic viscosity $v = 0.01$ has been performed on the same domain, with the same initial and boundary conditions. The time history of surface elevation, hydrodynamic pressure and velocity evolutions at the same control points are presented in Figure 12. Due to viscosity, the wave interactions are greater and determine great deformations in the wave period and great amplitude attenuations; as a consequence the transverse velocity component v almost vanishes after some time. In this case, the phenomenon is fully three dimensional at the beginning of the process and evolves into an almost two-dimensional phenomenon after some time. After the phenomenon gets two-dimensional (around non-dimensional time $t = 4$) the wave attenuation in time is small and is driven by the viscous effects.

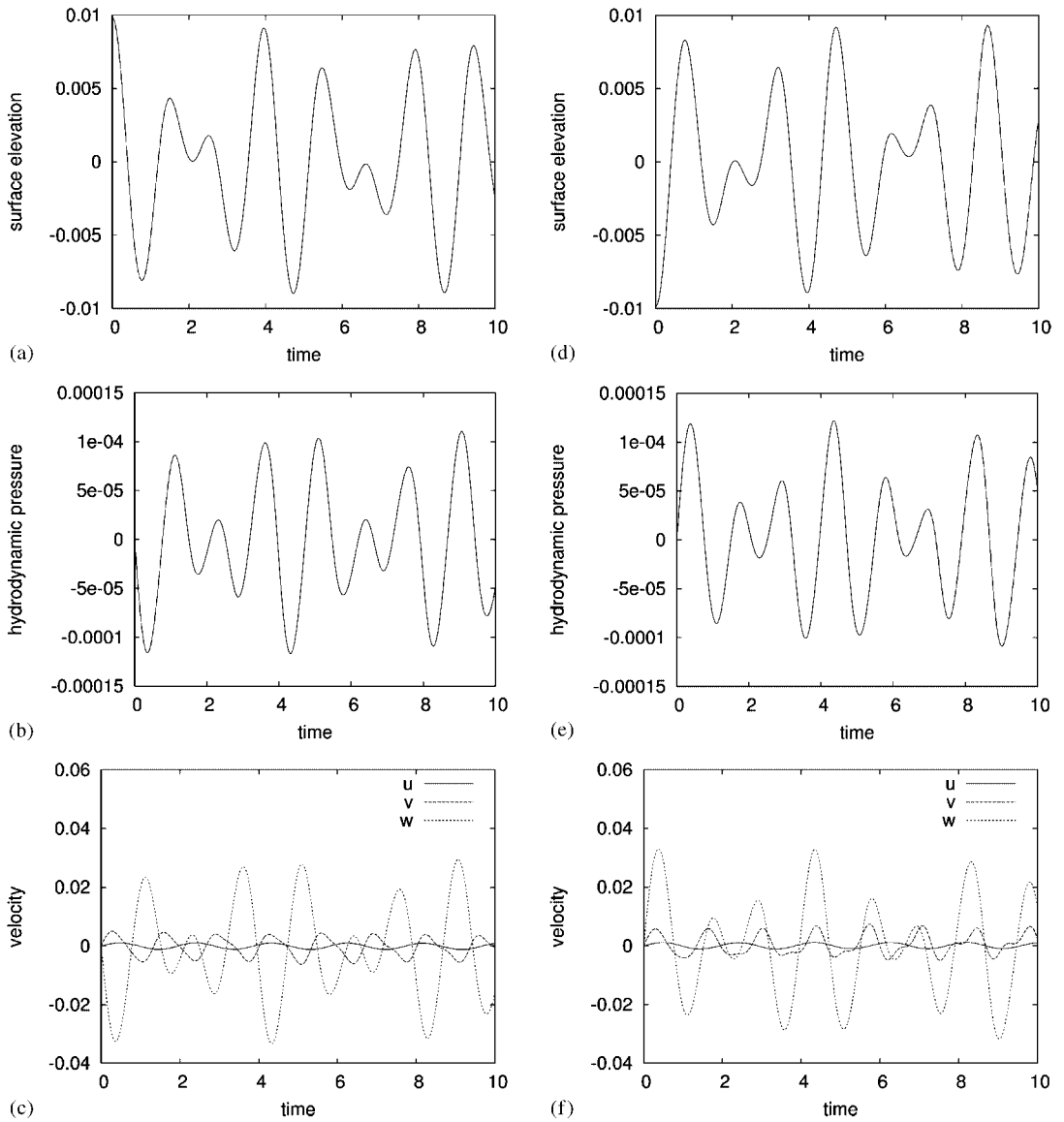

Figure 11. Three-dimensional oscillating basin without viscosity. Time history of the surface evolution at two control points: (a) $P1 \equiv (0.024, 0.042)$; and (d) $P2 \equiv (0.976, 0.458)$; time history of the hydrodynamic pressure and velocity fields at two control points (b,c) $P3 \equiv (0.024, 0.042, -0.025)$; and (e,f) $P4 \equiv (0.976, 0.458, -0.025)$, respectively.

6. CONCLUSIONS

The presented three-dimensional method for incompressible Navier–Stokes equations describes the hydrodynamic pressure field and the free surface evolution of environmental flows. The use

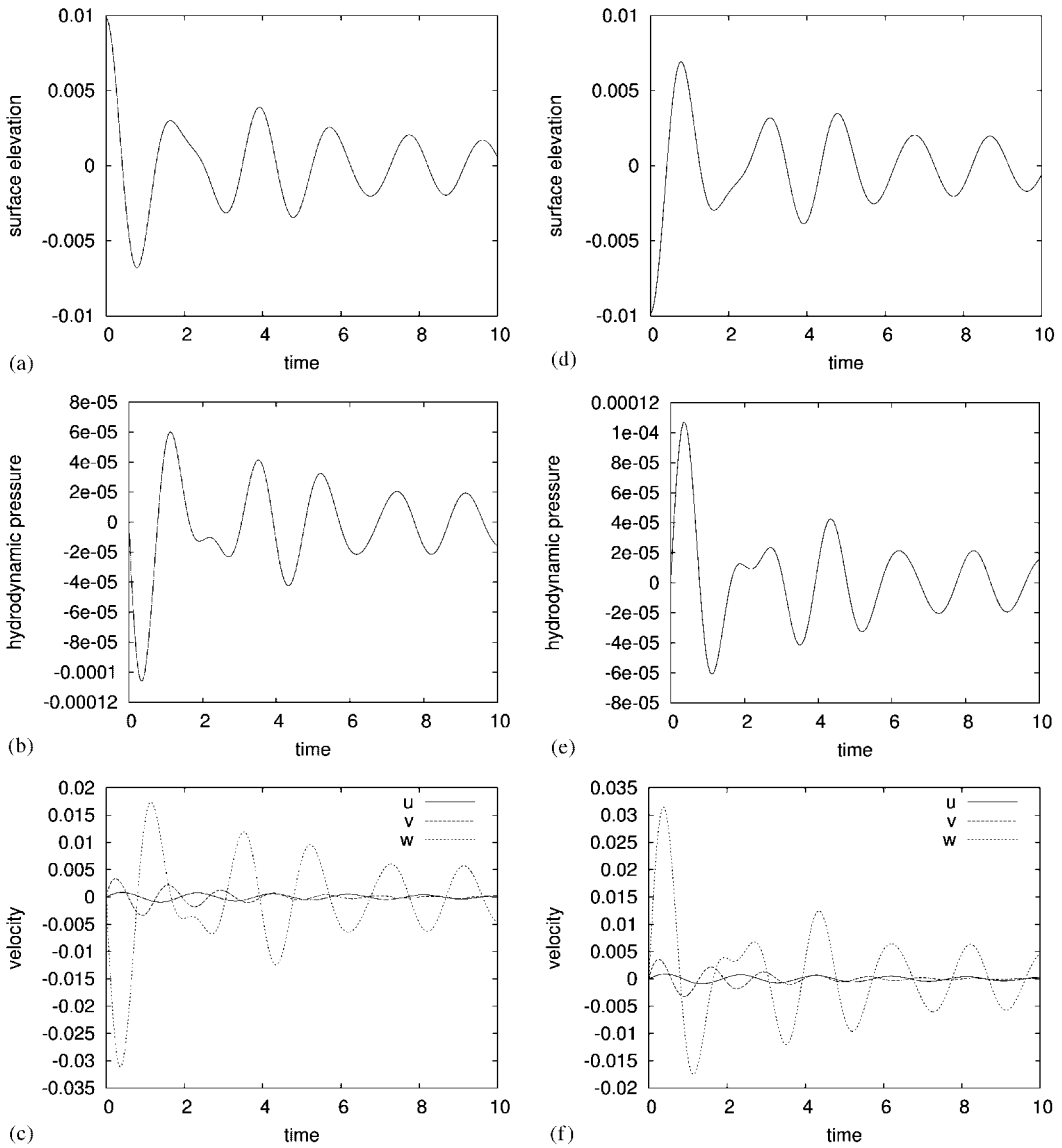

Figure 12. Three-dimensional oscillating basin in the presence of viscosity. Time history of the surface evolution at two control points: (a) $P1 \equiv (0.024, 0.042)$; and (d) $P2 \equiv (0.976, 0.458)$; time history of the hydrodynamic pressure and velocity fields at two control points (b,c) $P3 \equiv (0.024, 0.042, -0.025)$; and (e,f) $P4 \equiv (0.976, 0.458, -0.025)$, respectively.

of the finite volume method guarantees local and global mass conservation as demonstrated by the applications. The use of control volumes in the form of parallelepipeds and with variable heights at the surface is effective; indeed small mass losses are detected only when big surface

waves are considered. High-order approximations of the fluxes on the control volume faces and of the boundary conditions result in a good accuracy of the method, as demonstrated by the analytical test. The oscillating basin test demonstrates the accuracy and the stability of the model even in the presence of big wave amplitudes. Finally, the three-dimensional application shows that the model can effectively deal with fully three-dimensional, non-hydrostatic free surface flows.

In all the applications presented here Newtonian fluids have been considered; nevertheless the use of particular constitutive laws, e.g. Glen's law for ice, allows the description of the dynamics of non-Newtonian fluids [33]. The use of control volumes with inclined faces is also under study and its implementation should lead to an improved description of the free surface evolution and a better approximation of boundary conditions.

APPENDIX A

The convective term for the generic function ϕ on the control volume face is calculated as a function of ϕ-values at neighbouring points ϕ_i on the basis of the seven-point upwind stencil presented in Figure 1(a) with the following formula:

$$\phi_f = \sum_{i=1}^{7} C_i \phi_i \tag{A1}$$

with

$$\begin{aligned}
C_1 &= \frac{\xi_f(\xi_f - \xi_3)}{\xi_1(\xi_1 + \xi_3)} \\
C_2 &= 1 + \frac{\xi_f(\xi_3 - \xi_1 - \xi_f)}{\xi_1 \xi_3} - \frac{\Delta\eta^2}{12 y_4 \eta_5} - \frac{\Delta\zeta^2}{12\zeta_6\zeta_7} \\
C_3 &= \frac{\xi_f(\xi_1 + \xi_f)}{\xi_3(\xi_1 + \xi_3)} \\
C_4 &= \frac{\Delta\eta^2}{12\eta_4(\eta_4 + \eta_5)} \\
C_5 &= \frac{\Delta\eta^2}{12\eta_5(\eta_4 + \eta_5)} \\
C_6 &= \frac{\Delta\zeta^2}{12\zeta_6(\zeta_6 + \zeta_7)} \\
C_7 &= \frac{\Delta\zeta^2}{12\zeta_7(\zeta_6 + \zeta_7)}
\end{aligned} \tag{A2}$$

where ξ_i, η_i, ζ_i are the coordinates of neighbouring points P_i, $\Delta\xi$, $\Delta\eta$, $\Delta\zeta$ are the control volume dimensions and ξ_f, η_f, ζ_f are the coordinates of the point on the control volume face.

The diffusive term for the generic function ϕ on the control volume face is calculated as a function of ϕ-values at neighbouring points ϕ_i on the basis of the four-point central stencil presented in Figure 1(b) with the following formula:

$$\phi_f = \sum_{i=1}^{4} D_i \phi_i \tag{A3}$$

with

$$\begin{aligned} D_1 &= \frac{\xi_3^2}{4\xi_1(\xi_1+\xi_3)(\xi_1+\xi_4)} \\ D_2 &= -\frac{1}{\xi_3} - \frac{\xi_3}{4\xi_1\xi_4} \\ D_3 &= \frac{-4\xi_1\xi_3 - 3\xi_3^2 + 4\xi_1\xi_4 + 4\xi_3\xi_4}{4\xi_3(\xi_1+\xi_3)(\xi_4-\xi_3)} \\ D_4 &= \frac{\xi_3^2}{4\xi_4(\xi_3-\xi_4)(\xi_1+\xi_4)} \end{aligned} \tag{A4}$$

where ξ_i, η_i and ζ_i are the coordinates of neighbouring points P_i.

Further details on the calculation of diffusive and convective terms can be found in Reference [34].

ACKNOWLEDGEMENTS

The research grant provided to the first author by *Fondazione Fratelli Confalonieri* of Milano (Italy) is acknowledged. The authors are thankful to Samuel Hagos and Fabio Berta for the help on the analytical test.

REFERENCES

1. Gudmundsson GH. Basal-flow characteristic of a non-linear flow sliding frictionless over strongly undulating bedrock. *Journal of Glaciology* 1997; **43**(143):80–89.
2. Colinge J, Blatter H. Stress and velocity fields in glaciers: part I. Finite-difference schemes for higher-order glacier models. *Journal of Glaciology* 1998; **44**(148):448–456.
3. Lüthi MP, Funk M. Modelling heat flow in a cold, high-altitude glacier: interpretation of measurements from Colle Gnifetti, Swiss Alps. *Journal of Glaciology* 2001; **47**(157):314–324.
4. Pattyn F. Transient glacier response with a higher-order numerical ice-flow model. *Journal of Glaciology* 2003; **48**(162):467–477.
5. Deponti A, De Biase L, Pennati V. Thermal flow in glaciers: application to the Lys Glacier (Italian Western Alps). In *Advanced Computational Methods in Heat Transfer VIII*, Sundén B, Brebbia CA, Mendes AC (eds). WIT Press: Southampton, Boston, 2004; 69–75.
6. Pennati V, Corti S. Generalized Finite-Difference solution of 3D elliptical problems involving Neumann boundary conditions. *Communications in Numerical Methods in Engineering* 1994; **10**:43–58.
7. Feraudi F, Pennati V. Trasporto del Calore in Fluidi Incomprimibili: un Nuovo Approccio Numerico per Problemi Bidimensionali Non Stazionari. *L'Energia Elettrica* 1997; **74**(4):238–251.
8. Deponti A, Pennati V, De Biase L. A 3D FV method for alpine glaciers. In *Advanced Computational Methods in Heat Transfer VIII*, Sundén B, Brebbia CA, Mendes AC (eds). WIT Press: Southampton, Boston, 2004; 76–86.
9. Miller TF, Schmidt FW. Use of a pressure-weighted interpolation method for the solution of the incompressible Navier–Stokes equations on a nonstaggered grid system. *Numerical Heat Transfer* 1988; **14**:213–233.
10. Zang Y, Street RL, Koseff JR. A non-staggered grid, fractional step method for time-dependent incompressible Navier–Stokes equations in curvilinear coordinates. *Journal of Computational Physics* 1994; **114**:18–33.

11. Quarteroni A, Valli A. *Numerical Approximation of Partial Differential Equations*. Springer: Berlin, 1997.
12. Keshtiban IJ, Webster MF. A short note on pressure-correction schemes: TGPC and CBS. http://www-compsci.swan.ac.uk/reports/yr2005/CSR2-2005.pdf.
13. Leonard BP, Mokhtari S. ULTRA-SHARP solution of the Smith–Hutton problem. *International Journal of Numerical Methods for Heat and Fluid Flow* 1992; **2**:407–427.
14. Cordero E, De Biase L, Pennati V. A new finite volume method for the solution of convection–diffusion equations: analysis of stability and convergence. *Communications in Numerical Methods in Engineering* 1997; **13**:923–940.
15. De Biase L, Feraudi F, Pennati V. A finite volume method for the solution of convection–diffusion 2D problems by a quadratic profile with smoothing. *International Journal of Numerical Methods for Heat and Fluid Flow* 1996; **6**(4):3–24.
16. Leonard BP. Elliptic systems: finite-difference method IV. In *Handbook of Numerical Heat Transfer*, Minkowycz WJ (ed.). Wiley: New York; 1988.
17. Gresho PM. Some current CFD issues relevant to the incompressible Navier–Stokes equations. *Computer Methods in Applied Mechanics and Engineering* 1991; **87**:201–252.
18. Abdallah S. Comments on the Fractional Step Method. *Journal of Computational Physics* 1995; **117**:179–180.
19. Perot JB. Comments on the fractional step method. *Journal of Computational Physics* 1995; **121**:190–191.
20. Guermond JL, Quartapelle L. Calculation of incompressible viscous flows by an unconditionally stable projection FEM. *Journal of Computational Physics* 1997; **132**:12–33.
21. Hylin EC, McDonough JM. Derivation of projection methods from formal integration of the Navier–Stokes equations. *Journal of Computational and Applied Mathematics* 1997; **81**:349–374.
22. Blasco J, Codina R, Huerta A. A fractional-step method for the incompressible Navier–Stokes equations related to a predictor-multicorrector algorithm. *International Journal for Numerical Methods in Fluids* 1998; **28**:1391–1419.
23. Guermond JL, Quartapelle L. On stability and convergence of projection methods based on pressure Poisson equation. *International Journal for Numerical Methods in Fluids* 1998; **26**:1039–1053.
24. Casulli V. A semi-implicit finite difference method for non-hydrostatic, free-surface flows. *International Journal for Numerical Methods in Fluids* 1999; **30**:425–440.
25. De Foy B, Dawes W. Unstructured pressure-correction solver based on a consistent discretization of the Poisson equation. *International Journal for Numerical Methods in Fluids* 2000; **34**:463–478.
26. Armfield S, Street R. An analysis and comparison of the time accuracy of fractional-step methods for Navier–Stokes equations on staggered grids. *International Journal for Numerical Methods in Fluids* 2002; **38**:255–282.
27. Casulli V, Zanolli P. Semi-implicit numerical modeling of nonhydrostatic free-surface flows for environmental problems. *Mathematical and Computer Modelling* 2002; **36**:1131–1149.
28. http://netlib.org/alliant/ode/prog/cdrv.f and http://netlib.org/alliant/ode/prog/odrv.f
29. Ethier CR, Steinman DA. Exact fully 3D Navier–Stokes solution for benchmarking. *International Journal for Numerical Methods in Fluids* 1994; **19**:369–375.
30. Ramaswamy B. Numerical simulation of unsteady viscous free surface flow. *Journal of Computational Physics* 1990; **90**:396–430.
31. Ushijima S. Three-dimensional arbitrary Lagrangian–Eulerian numerical prediction method for non-linear free surface oscillation. *International Journal for Numerical Methods in Fluids* 1998; **26**:605–623.
32. Koçyigit MB, Falconer RA, Lin B. Three-dimensional numerical modelling of free surface flows with non-hydrostatic pressure. *International Journal for Numerical Methods in Fluids* 2002; **40**:1145–1162.
33. Deponti A, Pennati V, De Biase L, Maggi V, Berta F. A new fully 3D numerical model for ice dynamics. *Journal of Glaciology* 2005, submitted.
34. Deponti A. Mass and thermal flows in alpine glaciers. Application to Lys Glacier (Monte Rosa, Italia Alps). *Ph.D. Thesis*, Environmental Science Department, University of Milano-Bicocca, 2003.

